



An incompressible smoothed particle hydrodynamics method for the motion of rigid bodies in fluids



N. Tofghi^a, M. Ozbulut^a, A. Rahmat^a, J.J. Feng^{b,c}, M. Yildiz^{a,*}

^a Faculty of Engineering and Natural Sciences (FENS), Sabanci University, Orhanli, Tuzla, 34956 Istanbul, Turkey

^b Department of Mathematics, University of British Columbia, Vancouver, BC V6T 1Z2, Canada

^c Department of Chemical and Biological Engineering, University of British Columbia, Vancouver, BC V6T 1Z3, Canada

ARTICLE INFO

Article history:

Received 29 September 2014

Received in revised form 12 March 2015

Accepted 14 May 2015

Available online 15 May 2015

Keywords:

Smoothed particle hydrodynamics

Fluid–particle interaction

Sedimentation

Fictitious domain

Viscous penalty

ABSTRACT

A two-dimensional incompressible smoothed particle hydrodynamics scheme is presented for simulation of rigid bodies moving through Newtonian fluids. The scheme relies on combined usage of the rigidity constraints and the viscous penalty method to simulate rigid body motion. Different viscosity ratios and interpolation schemes are tested by simulating a rigid disc descending in quiescent medium. A viscosity ratio of 100 coupled with weighted harmonic averaging scheme has been found to provide satisfactory results. The performance of the resulting scheme is systematically tested for cases with linear motion, rotational motion and their combination. The test cases include sedimentation of a single and a pair of circular discs, sedimentation of an elliptic disc and migration and rotation of a circular disc in linear shear flow. Comparison with previous results at various Reynolds numbers indicates that the proposed method captures the motion of rigid bodies driven by flow or external body forces accurately.

© 2015 Elsevier Inc. All rights reserved.

1. Introduction

The interaction of a solid structure with a fluid environment is common in nature and industry. Such interaction occurs when solid objects move in a fluid environment. Examples include airfoils [1], flexible bodies [2,3], impacting solids [4–6], rigid and deformable particles [7–9] and blood cells [10,11]. Another type of fluid–solid interaction involves fluids moving in deformable solid boundaries such as blood vessels and heart chambers [12,13].

From a mathematical and numerical standpoint, computational fluid dynamics methods have conventionally employed an Eulerian perspective while computational solid mechanics are generally described in a Lagrangian framework. The coupling schemes between the two may be loosely grouped as those that rely on specific boundary conditions and those that introduce external terms into Navier–Stokes (NS) equations [14]. An example of the former is Arbitrary Lagrangian–Eulerian (ALE) [15,16] method while Immersed Boundary (IB) and Fictitious Domain (FD) follow the latter approach. IB method satisfies the boundary conditions in the vicinity of the solid body by introducing a local forcing term near these boundaries [12, 17–20]. An extensive review of IB method has been provided in [21]. On the other hand, FD method imposes a constraint to recover solid-body motion in the entire region occupied by the solid. One such scheme is the Distributed Lagrangian Multiplier (DLM) method [2,3,22–24]. Another class of FD uses a penalization term to induce rigid motion. Such a penalty

* Corresponding author.

E-mail addresses: meyildiz@sabanciuniv.edu, myildiz@uvic.ca (M. Yildiz).

may come as a new term added to the NS equations, as in the Brinkman penalization [25,26], or as a modification to an existing term, as in the Viscous Penalty (VP) method that augments the viscous dissipation in the NS equation [9,27,28].

The more established fluid–solid simulation methods mentioned above rely on an underlying fluid mesh that may be moved or refined to adapt to the moving boundaries of the solid. This typically produces complex algorithms. An alternative would be to discretize both fluid and solid using a particle-based scheme. These particles move in a Lagrangian fashion and the fluid–solid interaction is realized naturally. Such a meshless scheme has an inherent advantage over conventional mesh-based methods. By proper initialization of particle positions, one may trace all the moving boundaries without additional treatment [29]. A review of different particle methods has been provided in [30]. One such Lagrangian method is Smoothed Particle Hydrodynamics (SPH), developed by Lucy [31] and Gingold and Monaghan [32]. SPH has been used extensively to study the fluid–solid interaction in the vicinity of a free surface and is known for its ability to capture intricate physics of the problem. Impact of rigid bodies [4–6,33], wave interaction of floating bodies [34] and sloshing motion [35,36] are examples of such flows.

In contrast, SPH has rarely been applied to an important class of fluid–solid coupling problems: particulate two-phase flows that involve motion of solid particles in a surrounding fluid medium. Two studies [37,38] have dealt with solid bodies with prescribed motion using Weakly Compressible SPH (WCSPH). Hashemi et al. [39] have used WCSPH to simulated particle sedimentation using a modified pressure boundary condition. Bian et al. [40] have applied WCSPH to concentrated particle suspensions. Implementing WCSPH requires subtle treatment of its various components. For instance, an artificial equation of state and a speed of sound need to be chosen to enforce incompressibility. Corrective numerical treatments such as density filtering may be necessary to alleviate oscillation in the pressure field, and numerical stability often dictates small time steps [41,42]. Thus, more extensive studies are needed in SPH simulation of particulate flows, and development of Incompressible SPH (ISPH) methods is of special interest in this area.

Given the scientific and practical significance of particulate flows, they have been among the first test cases for mesh-based fluid–solid coupling methods in the past. Feng et al. have examined the sedimentation of circular and elliptical particles [43] and the motion said particles in Poiseuille and Couette flows [44]. These have been used as benchmark problems by many authors for FD/DLM, IB and lattice-Boltzmann methods, among others [22,45]. Yan et al. [46] studied the interaction of a pair of circular particles in simple shear flow while Pan et al. [24] focused on the migration of circular particles in the same flow pattern. Ding and Aidun [47] investigated the rotation of circular and elliptical particles in Couette flow. Xia et al. [48] focused on the sedimentation of an elliptic particle in vertical channel and its interaction with bounding walls.

The objective of this work is to develop an accurate and robust SPH scheme for simulating motion of solid particles in a Newtonian fluid. Our two-dimensional ISPH scheme is based on the projection method [49] and uses the VP approach [9,27] to realize rigid-body motion in the solid regions. This avoids the complications in other forms of boundary implementation in SPH. Additionally, a rigidity constraint is imposed to preserve the relative position of the particles belonging to the solid phase [33,50], especially in the transition region between fluid and solid phases. In order to avoid contact between rigid bodies, a repulsive force is formulated based on the relative position of individual SPH particles. The resulting scheme is extensively tested in five cases involving the linear motion, rotational motion and their combinations for one or two particles in two dimensions. These problems were chosen because of comparable results in the literature. But the scheme can be generalized in a straightforward way to a multiphase SPH solver for many embedded solid particles.

The rest of the paper is structured as follows. Governing equations and numerical procedures are presented in Section 2, simulation results are shown in Section 3 and concluding remarks are drawn in Section 4. For distinction, the solid objects will be called discs while the SPH particles will be simply referred to as particles.

2. Mathematical formulation

2.1. Governing equations

Equations governing an incompressible flow may be written in dimensionless form as

$$\nabla \cdot \mathbf{u} = 0, \quad (1)$$

$$\rho \frac{D\mathbf{u}}{Dt} = -\nabla p + \frac{1}{Re} \nabla \cdot \boldsymbol{\tau}, \quad (2)$$

where ρ is density, \mathbf{u} is the velocity vector, p is pressure, t is time and $D/Dt = \partial/\partial t + \mathbf{u} \cdot \nabla$ represents the material time derivative. Here, $\boldsymbol{\tau}$ and Re are the viscous stress tensor and Reynolds number, respectively. The viscous stress tensor is defined as

$$\boldsymbol{\tau} = \mu \left[\nabla \mathbf{u} + (\nabla \mathbf{u})^\dagger \right], \quad (3)$$

where μ denotes the dynamic viscosity and superscript \dagger represents the transpose operation. Dimensionless values are formed using the following scales

$$\begin{aligned} \mathbf{x} &= \mathbf{x}^*/l_c, \quad \rho = \rho^*/\rho_f, \quad \mu = \mu^*/\mu_f, \quad \mathbf{u} = \mathbf{u}^*/u_c, \quad t = t^*(u_c/l_c), \\ p &= (p^* - \rho^* \mathbf{g} \cdot \mathbf{x}^*)/0.5\rho_f u_c^2, \quad \mathcal{D} = \rho_s/\rho_f, \quad \mathcal{V} = \mu_s/\mu_f, \end{aligned} \quad (4)$$

leading to a Reynolds number defined as

$$Re = \frac{\rho_f u_c l_c}{\mu_f}, \quad (5)$$

where \mathbf{x} is the position vector, \mathbf{g} is the constant gravitational acceleration vector and l_c and u_c denote characteristic length and velocity, respectively. An asterisk marks dimensional variables whereas subscripts \square_s and \square_f denote fluid and solid phases, respectively.

2.2. Fluid–solid coupling scheme

To distinguish between different phases, a color function \hat{c}^α is defined for each phase α such that it assumes a value of unity for phase α and zero for the others. The color function is then smoothed out across the phase boundaries over all neighboring particles J_n as

$$c_i^\alpha = \frac{1}{\psi_i} \sum_{j=1}^{J_n} \hat{c}_j^\alpha W_{ij} \quad (6)$$

to ensure smooth transition between the properties of each phase when used for their interpolation. W_{ij} is a shortened notation for the interpolation kernel $W(r_{ij}, h)$. The interpolation kernel is a function of the magnitude of distance vector, $\mathbf{r}_{ij} = \mathbf{r}_i - \mathbf{r}_j$, between particle of interest i and its neighboring particles j and h , the smoothing length taken 1.6 times the initial particle spacing. Here $\psi_i = \sum_{j=1}^{J_n} W_{ij}$ is the number density of particle i . Having a compact support of two smoothing lengths, a cubic spline kernel [51] is used to calculate the smoothed color function which results in a transition region covering four particle spacings across the interface.

Interpolation of phase properties for a single fluid phase, of color c_i , and multiple solid phases may be carried out as Weighted Arithmetic Mean (WAM),

$$\phi_i = \sum_{\alpha} \phi_s^\alpha c_i^\alpha + \phi_f c_i, \quad (7)$$

or Weighted Harmonic Mean (WHM),

$$\frac{1}{\phi_i} = \sum_{\alpha} \frac{c_i^\alpha}{\phi_s^\alpha} + \frac{c_i}{\phi_f}, \quad (8)$$

where ϕ may denote viscosity or density, where appropriate.

All phases are treated as liquids and are evolved through Eqs. (1) and (2). In addition, the solid phase is assigned a much higher viscosity such that it approximates a rigid body [9]. However, due to the diffuse interface employed here, the solid particles that have fluid particles in their support domain will experience a deficit in viscosity. As a result, these solid particles will act in a fluid-like fashion and drift apart without further treatment. In this study, we implement an additional constraint derived from the conservation of momenta in a rigid body to treat the solid particles [50]. To impose these constraints, we use the current velocity of the solid particles to compute a center-of-mass velocity and an angular velocity for the solid object:

$$\mathbf{u}_s^t = \frac{1}{M_s} \sum_{j=1}^{J_s} \frac{\mathbf{u}_j}{\psi_j}, \quad (9)$$

$$\mathbf{u}_s^r = \frac{1}{I_s} \sum_{j=1}^{J_s} \frac{\mathbf{u}_j \times \mathbf{r}_{js}}{\psi_j}, \quad (10)$$

and then assign an individual velocity to each solid particle according to rigid body motion:

$$\mathbf{u}_i = \mathbf{u}_s^t + \mathbf{u}_s^r \times \mathbf{r}_{is}. \quad (11)$$

Here, $\mathbf{r}_{is} = \mathbf{r}_i - \mathbf{r}_s$ where \mathbf{r}_s denotes the solid object's center of mass and J_s is the total number of particles present in the solid phase. As density remains constant for particles of the solid phase, M_s and I_s represent the rigid body's volume and moment of inertia about its center of mass as

$$M_s = \sum_{j=1}^{J_s} \frac{1}{\psi_j}, \quad I_s = \sum_{j=1}^{J_s} \frac{r_{js}^2}{\psi_j}. \quad (12)$$

Coupling the viscous penalty and rigidity constraint in an SPH framework enables the particles to maintain rigid behavior inside the body through the increased viscosity. At the same time, the relative positions of the rigid body particles, especially in the transition region where the viscosity is smaller, are maintained using the rigidity constraints. As a result, the scheme proposed here imposes little computational overhead while circumventing explicit boundary condition implementations.

2.3. Spatial and temporal discretization

Employing Taylor series expansion in conjunction with the properties of the kernel function, the first derivative of an arbitrary function may be put into discrete form as

$$\frac{\partial f_i^m}{\partial x_i^k} a_i^{kl} = \sum_j \frac{1}{\psi_j} (f_j^m - f_i^m) \frac{\partial W_{ij}}{\partial x_i^l}, \quad (13)$$

while Laplace operators for vectorial and scalar quantities are approximated as

$$\frac{\partial}{\partial x_i^k} \left(\varphi_i \frac{\partial f_i^m}{\partial x_i^k} \right) a_i^{ml} = 8 \sum_j \frac{\varphi_{ij}}{\psi_j} (f_i^m - f_j^m) \frac{r_{ij}^m}{r_{ij}^2} \frac{\partial W_{ij}}{\partial x_i^l}, \quad (14)$$

$$\frac{\partial}{\partial x_i^k} \left(\varphi_i \frac{\partial f_i}{\partial x_i^k} \right) [2 + a_i^{kk}] = 8 \sum_j \frac{\varphi_{ij}}{\psi_j} (f_i - f_j) \frac{r_{ij}^k}{r_{ij}^2} \frac{\partial W_{ij}}{\partial x_i^k}, \quad (15)$$

respectively, where

$$\varphi_{ij} = \frac{2\varphi_i\varphi_j}{\varphi_i + \varphi_j}, \quad (16)$$

$$a_i^{ml} = \sum_j \frac{r_{ij}^m}{\psi_j} \frac{\partial W_{ij}}{\partial x_i^l}. \quad (17)$$

Here, \mathbf{a}_i is a corrective second rank tensor which serves to eliminate particle inconsistencies arising from discrete form of the kernel function [52]. A quintic spline kernel [53,54] has been used to ensure accurate calculation of derivatives and robustness of the scheme.

A predictor–corrector scheme [49] is employed to advance the discretized equations in time using a first-order Euler approach. The Courant–Friedrichs–Lewy (CFL) condition [55],

$$\Delta t = \gamma \min_{1 \leq j \leq J_d} \left(\frac{h}{u_j}, \frac{1}{Re} \frac{h^2 \rho_j}{2\mu_j} \right), \quad (18)$$

is used to determine the timestep of the simulation. Here γ is taken to be equal to 0.25 [56] while J_d denotes all particles within the computational domain. In the predictor step, particles are displaced to their intermediate positions using

$$\mathbf{r}_i^+ = \mathbf{r}_i^{(n)} + \mathbf{u}_i^{(n)} \Delta t + \delta \mathbf{r}_i^{(n)}, \quad (19)$$

followed by an update in transport properties due to movement of the interface. Here, \square^+ represents an intermediate value and superscript (n) denotes values at the n th time step. Artificial particle displacement, applied only to particles within the fluid region of the flow, is implemented through $\delta \mathbf{r}_i^{(n)}$ as

$$\delta \mathbf{r}_i^{(n)} = \zeta \left[\max_{1 \leq k \leq J_d} (u_k) \sum_{j=1}^{J_n} \left(\frac{\mathbf{r}_{ij}}{r_{ij}^3} r_{av,i}^2 \right) \right]^{(n)} \Delta t, \quad (20)$$

which ensures orderly particle distribution, improving the robustness of the scheme [52,57]. Average particle spacing is found via $r_{av,i} = \sum_j r_{ij} / J_n$ while a value of $\zeta = 0.06$ is employed throughout this study to ensure satisfactory particle distribution and stabilizing effect [56].

Intermediate velocities are found by calculating the right-hand side of Eq. (2) excluding pressure gradients at the intermediate particle locations as

$$\mathbf{u}_i^+ = \mathbf{u}_i^{(n)} + \frac{1}{\rho_i^{(n)} Re} \nabla \cdot \boldsymbol{\tau}_i^{(n)} \Delta t, \quad (21)$$

while intermediate densities are calculated employing the following relations

$$\psi_i^+ = \psi_i^{(n)} - \Delta t \psi_i^{(n)} (\nabla \cdot \mathbf{u}_i^+), \quad (22)$$

$$\rho_i^+ = m_i \psi_i^+. \quad (23)$$

In the corrector step, pressure at the next timestep is found by solving Poisson equation subject to zero gradient boundary condition using intermediate values,

$$\nabla \cdot \left(\frac{1}{\rho^+} \nabla p^{(n+1)} \right) = \frac{\nabla \cdot \mathbf{u}^+}{\Delta t}, \quad (24)$$

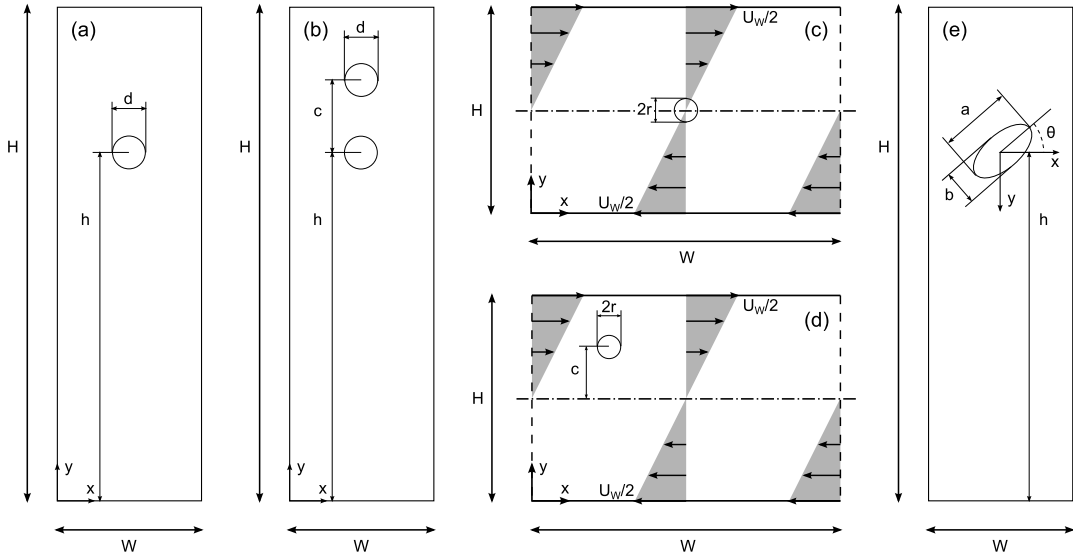


Fig. 1. Schematics and coordinate axes of all test cases included in this study; (a) SDD (Single Disc Descent); (b) DDD (Double Disc Descent); (c) SDR (Single Disc Rotation); (d) SDM (Single Disc Migration); (e) SED (Single Ellipse Descent).

which is then employed to correct the velocity of the particles, hence advancing them to next timestep using the following relation,

$$\mathbf{u}_i^{(n+1)} = \mathbf{u}_i^+ - \frac{1}{\rho_i^+} \nabla p_i^{(n+1)} \Delta t. \quad (25)$$

At this point, rigidity constraints of Eqs. (9)–(11) are imposed on the velocity vector values at the next time step. This temporarily violates the incompressibility condition at the transition region in the current time step as the effects of rigid body movement on the fluid phase are delayed until next time step [50]. Finally, particles are moved to their corrected positions using the following relation,

$$\mathbf{r}_i^{(n+1)} = \mathbf{r}_i^{(n)} + \frac{1}{2} (\mathbf{u}_i^{(n)} + \mathbf{u}_i^{(n+1)}) \Delta t + \delta \mathbf{r}_i^{(n)}, \quad (26)$$

and number density values are restored to that of the previous timesteps.

All boundary conditions at stationary walls are applied using multiple boundary tangent method [58].

3. Results

This section reports numerical results for the five test cases, each given an acronym: SDD (Single Disc Descent), DDD (Double Disc Descent), SDR (Single Disc Rotation), SDM (Single Disc Migration) and SED (Single Ellipse Descent). Schematics and coordinate axes for all cases are presented in Fig. 1. The effects of spatial resolution J_d and γ constant in the CFL condition are studied for all test cases and sample results for SDD and SDR are provided. Unless otherwise noted, all results are presented in dimensionless forms obtained from characteristic scales provided in the respective section.

3.1. Single disc descent

The proposed scheme for simulation of motion of rigid bodies treats all phases as liquids of different viscosities initially, only to differentiate the solid phase by the rigid-body constraints (9)–(11) afterwards. As such, the viscosity ratio between the phases and the method of transition have significant effects on the results obtained [9,27]. To identify a suitable range for \mathcal{V} and choose the appropriate interpolation scheme, several simulations of a rigid disc descending from rest under gravity in quiescent fluid have been conducted. Characteristic length and velocity are chosen as $l_c = d$ and $u_c = \sqrt{gd}$ (refer to Fig. 1(a)) while dimensionless numbers governing this case are $Re_p = \rho_f \sqrt{gd^3} / \mu_f$, h/d , \mathcal{D} and \mathcal{V} .

The computational domain consists of an 8×24 rectangle with no-slip and no penetration boundary conditions applied at bounding walls. Particles discretizing the rigid body conform to the boundaries and are positioned along concentric circles at uniform radial spacing around the rigid disc's center. The radial spacing is chosen such that certain number of circles, depending on the target resolution, fit inside the disc while the number of particles along each of these circles vary to keep the overall inter-particle spacing roughly uniform. Fluid particles are arranged on a uniformly spaced Cartesian grid (Fig. 2(a)). It is evident that the particle arrangement in the vicinity of the rigid body is initially non-uniform, however,

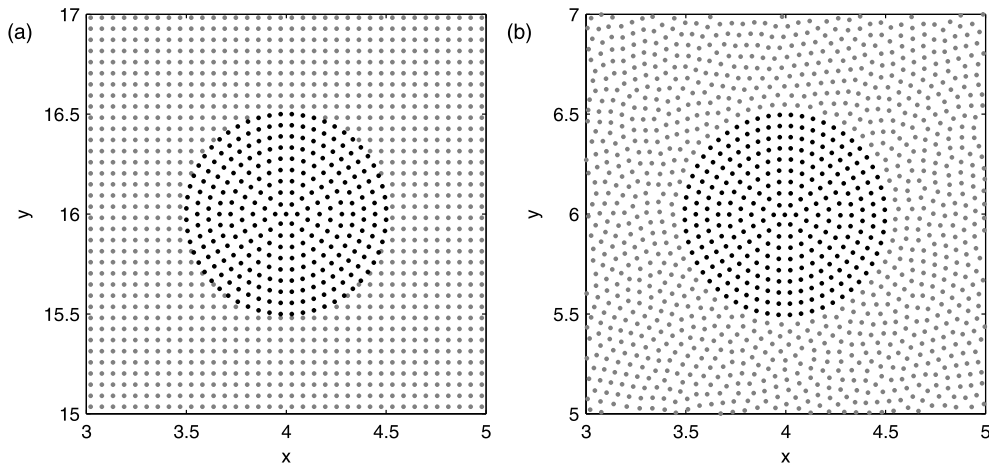


Fig. 2. Closeup view of initial particle distribution in the vicinity of the solid disc. Black points denote solid particles whereas gray points are fluid particles. (a) Initial arrangement; (b) particle positions at $y = 6$.

Table 1

Vertical position and vertical velocity of the rigid disc's center at $t = 30$ for different viscosity and interpolation schemes. WAM and WHM interpolation schemes are defined in Eqs. (7) and (8), respectively. (Refer to [59] for detailed discussion.)

\mathcal{V}	1	3	10	30	100	300	1000	100
Int.	WHM	WHM	WHM	WHM	WHM	WHM	WHM	WAM
y	6.6035	6.8568	6.9818	7.0091	7.0217	7.0279	7.0262	7.8529
u_y	−0.3703	−0.3611	−0.3578	−0.3567	−0.3565	−0.3564	−0.3562	−0.3217

this deficiency is quickly remedied in the current scheme. A uniform particle spacing is achieved as artificial particle displacement and incompressibility condition adapt the initial arrangement to the test case geometry (Fig. 2(b)) [57]. A fully uniform initial arrangement has also been simulated to test the possible effects of such initial defects and no significant differences in the results were observed between the two initial arrangements.

To test how \mathcal{V} and the viscosity interpolation scheme affect the results, we tabulate in Table 1 the instantaneous vertical position y and vertical velocity u_y of the disc at $t = 30$. Reynolds number is set to 39.1, h/d is equal to 16 and a density ratio of 1.25 is chosen. The solution is expected to converge to that of a solid disc with increasing viscosity ratio. When using WHM interpolation scheme, the results show such behavior after $\mathcal{V} > 30$. As for WAM, viscosity ratios up to 100 are tested (not shown here), however, no convergence was observed. This is an expected outcome as WHM skews the transition region toward the interior of the rigid body, leaving the lower viscosity fluid region almost unaltered. Based on these observations, it may be inferred that a viscosity ratio of $\mathcal{V} = 100$ along with WHM interpolation scheme produces satisfactory results. (Refer to [59] for detailed discussion.) These values along with the initial particle arrangement method are used throughout the simulations conducted in this study, unless noted otherwise.

Fig. 3 provides simulation results at different spatial resolutions J_d and γ constants of the CFL condition. When released from rest, all cases undergo an initial acceleration, followed by descent at more or less constant velocity, and finally a deceleration when approaching the bottom boundary. Figs. 3(a) and 3(b) show vertical position and vertical velocity of the rigid disc's center of mass for total number of particles (in parentheses: number of concentric circles inside the rigid body) of 23 234 (5), 37 650 (7), 62 230 (10) and 119 986 (13) at $\gamma = 0.25$. While the difference in position increases at later stages of the simulation, the difference between the two cases of highest resolution remains below 1% of the maximum drop height till the end of simulation. Similarly, the velocity agrees within 2% of the maximum descent velocity between the three highest resolutions. Furthermore, the initial stages of the simulation ($t < 10$) for $J_d = 119 986$ and $J_d = 62 230$ show identical velocity profiles. As a result, we consider the solution converged with respect to spatial resolution for $J_d = 62 230$. The effects of γ on vertical position and vertical velocity of the disc's center of mass for $J_d = 62 230$ are shown in Figs. 3(c) and 3(d). The difference between position and velocity for $\gamma = 0.125$ and $\gamma = 0.25$ is less than 1% while the disc descends slower when $\gamma = 0.5$.

Based on the differences observed for the resolutions tested above, the middle case is chosen for comparison with WCSPH results of Hashemi et al. [39] and DLM simulations of Glowinski et al. [22]. The results for vertical position and vertical velocity are presented in Fig. 4. There is excellent agreement overall. If we inspect their differences more closely, the current method overestimates the vertical position of the disc during the simulation. But the difference in the settling velocity is subtler. Simulations by Hashemi et al. and Glowinski et al. agree better during the acceleration stage while SDD predicts a slower descent. However, the terminal velocities predicted by SDD are in better agreement with DLM results while

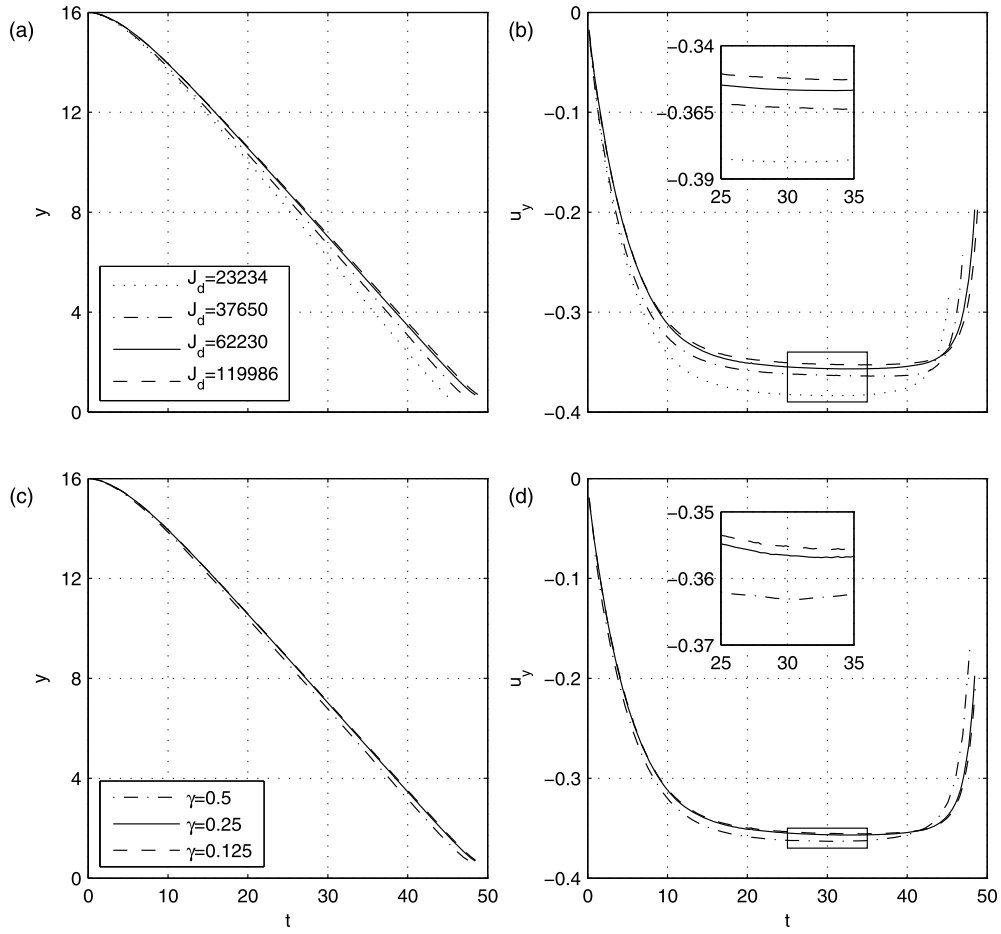


Fig. 3. Comparison of simulation results for the rigid disc's center of mass of case SDD; vertical position (a) and vertical velocity (b) for different J_d and $\gamma = 0.25$; vertical position (c) and vertical velocity (d) for different γ and $J_d = 62230$.

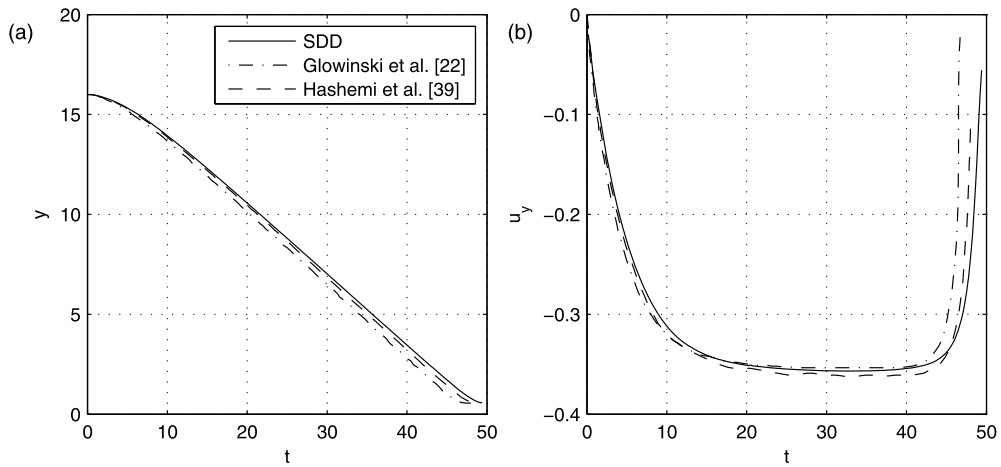


Fig. 4. Comparison of simulation results with literature data; (a) vertical position; (b) vertical velocity.

WCSPH overestimates the terminal velocity. The final deceleration stage is the most varied stage as DLM starts to experience boundary effects before others while SDD shows such effects the last. Based on these results, the proposed method shows quantitative agreement with the numerical results provided by [22,39] for the overall duration of the simulation.

Table 2Minimum distance between disc surfaces for different c_r . Negative values in distance denote crossover.

$c_r (\times 10^5)$	40	16	8	5.33	4	0.8	0.4	0.04
$\min\left(\frac{c-d}{d}\right)$	0.0659	0.0524	0.0408	0.0321	0.0254	−0.0253	−0.0449	−0.656

Table 3

Dimensionless parameters for DDD cases.

Case	Re_p	\mathcal{D}	J_d	$H \times W$	c/d	h/d
DDD1	56	1.1	62 226	30×10	2	25
DDD2	391.3	1.5	74 846	24×8	2	18

3.2. Double disc descent

In this section, the interaction between two rigid discs descending in quiescent fluid is studied. This test case will help measure the success of the proposed method in handling multiple bodies and the interaction of interpolation regions. To this end, two rigid discs with equal diameter are placed such that the line connecting the centers of the discs is parallel to the vertical walls and has a length c . A schematic of the test case is shown in Fig. 1(b) while initial particle positions are similar to SDD. The characteristic parameters are identical to SDD and the problem is fully described by specifying domain size, h/d , Re_p , \mathcal{D} and an additional parameter, c/d .

It is known that when released from rest, the discs will undergo Drafting–Kissing–Tumbling (DKT) motion [43]. The following disc catches up with the leading one and they attain a near-contact configuration. However, this configuration is unstable and a rotational motion will ensue which results in the pair breaking off and drifting apart. A repulsive force is employed in near-contact cases to ensure a safe distance between the rigid bodies and avoid crossover of solid particle of different phase. Such repulsive forces have been extensively used in literature and take different forms such as lubrication force [48,60] and spring force [22,45,48,61]. Here, an adapted form of the spring force benefiting from the Lagrangian nature of the discretization method is developed. It relies on the color and distance data available to individual particles without prior knowledge of the body geometry. Denoting the particle spacing by δ_p and the force coefficient by c_r , the repulsive force applied to the particle i of rigid body α due to its proximity with rigid body β may be formulated as

$$\mathbf{f}_{i(r)}^\alpha = c_r \left(\frac{c_i^\beta}{c_i^\alpha} \right)^2 \sum_{j=1}^{J_n} \frac{\mathbf{r}_{ij} \hat{c}_j^\beta}{\delta_p}, \quad (27)$$

which will be added to the right-hand side of Eq. (21) as $\mathbf{f}_{i(r)}^\alpha \Delta t / \rho_s$. Note that this force is only non-zero when particle i of phase α has a particle of phase β in its support domain so that $c_i^\beta > 0$. As the distance between the two discs decreases, $\mathbf{f}_{i(r)}^\alpha$ increases due to larger c_i^β . In the above formulation c_r should be chosen such that the minimum distance between the discs is limited to approximately one particle spacing. Here, c_r is varied as shown in Table 2 to find the suitable value. The repulsive force is tested by simulating DDD with $Re_p = 56$, $\mathcal{D} = 1.1$, $h/d = 25$ and $c/d = 2$ in a 30×10 computational domain discretized by 62 226 particles. The minimum distance between disc surfaces provided in Table 2 shows that for the values of c_r tested here, a crossover happens for $c_r \leq 8 \times 10^4$. To maintain a minimum separation comparable to the particle spacing $\delta_p/d = 0.0625$ for this resolution, $c_r = 1.6 \times 10^6$ is chosen. Using the repulsive force described above, DDD at two different Re_p are compared to numerical results provided by Hashemi et al. [39] and Glowinski et al. [22]. Simulation parameters for each case are presented in Table 3. DDD at low and high Re_p are referred to as DDD1 and DDD2, respectively.

Fig. 5 compares the vertical position and vertical velocity of DDD1 with the WCSPPH results of [39]. Kissing stage starts when velocities of the discs converge while onset of tumbling is when the velocities start to drift apart. Tumbling happens when the vertical positions of the discs cross. Prior to the tumbling stage, the two solutions agree closely. However, the onset of tumbling and the subsequent disc velocities differ somewhat from those found in [39]. It should be noted that in both numerical simulations the kissing and tumbling stages are highly sensitive to the repulsive force employed [62]. As a result, the difference in tumbling stage between DDD1 and [39] is to be expected. To assess the performance of the proposed scheme at higher Re_p , simulation results of DDD2 are compared to those of [22] in Fig. 6. The current method slightly overestimates the position of the discs when compared to [22]. As for the velocity, the general features of the pair until kissing stage, such as the crossover between velocity curves of top and bottom discs at about $t \approx 6$ or bouncing motion observed at $t \approx 10$, are accurately captured. However, due to the same reason mentioned for DDD1, the quantitative values are different from [22] after $t \approx 10$ when kissing and tumbling stages are in progress. Taken as a whole, the comparison above shows that the current method is able to capture the essential characteristics of DKT up to the Re_p tested here.

3.3. Single disc rotation

In order to isolate the angular motion and assess the performance of the proposed method in the absence of linear motion, rotation of a neutrally buoyant, single rigid disc suspended in Couette flow is simulated and the results are compared

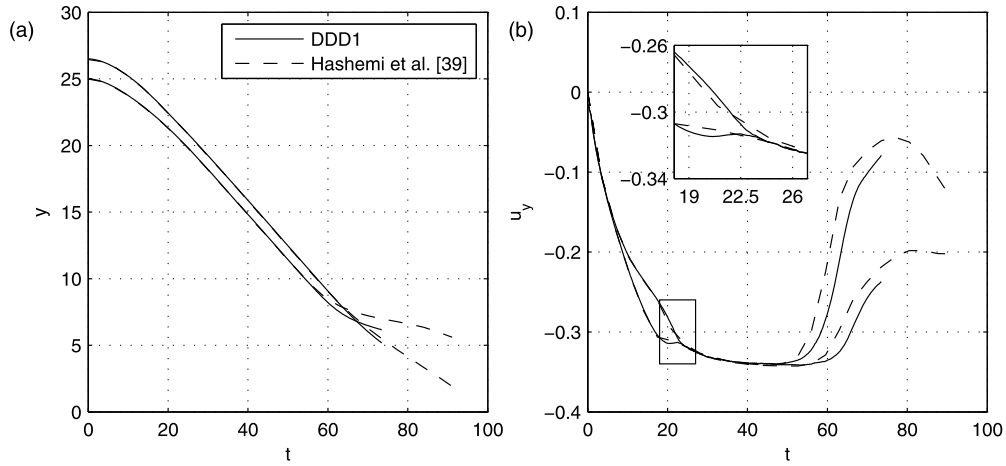


Fig. 5. Comparison of simulation results at $Re_p = 56$; (a) vertical position; (b) vertical velocity.

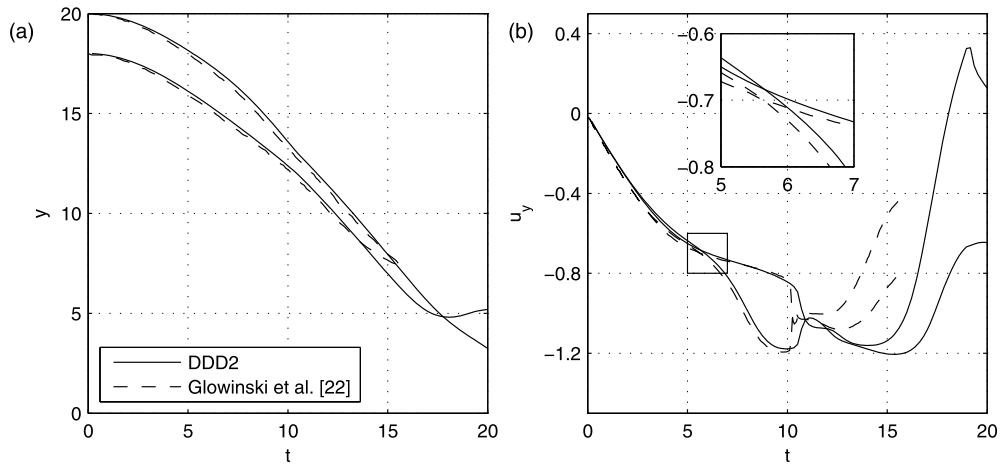


Fig. 6. Comparison of simulation results at $Re_p = 391.3$; (a) vertical position; (b) vertical velocity.

with the data available in literature. This test case has been subject to extensive experimental and numerical investigation, spanning a wide range of Reynolds numbers [24,46,47]. A schematic of this case is provided in Fig. 1(c). Denoting the shear rate of the undisturbed flow by G such that $U_w = GH$, we define the bulk Reynolds number $Re_b = \rho_f GH^2 / \mu_f$, particle Reynolds number $Re_p = \rho_f Gr^2 / \mu_f$ and confinement ratio H/r . A pair of these dimensionless numbers would suffice to define the test cases.

A series of simulations with increasing Re_p have been conducted for $H/r = 4$. Horizontal walls are set to move at $U_w/2$ in opposite directions while no slip and no penetration boundary conditions are applied. The computational domain extends up to $8r$ on both sides of the disc in streamwise direction ending in periodic boundaries. The rigid disc is placed at the center of the computational domain at rest while fluid particles are initialized with the analytical velocity of Couette flow with respect to their initial position. Initial particle arrangement is similar to case SDD. Fig. 7(a) depicts the dimensionless angular velocity ω/G at three different spatial resolutions with total number of particles (in parentheses: number of concentric circles inside the rigid body) of 6389 (10), 14385 (15) and 32435 (23) for $\gamma = 0.25$. The resolution is kept the same for all Re_p . Considering consecutive levels of resolution, the simulation with lower resolution predicts larger ω/G at either end of the Re_p spectrum. Comparing with $J_d = 14385$, lowest resolution shows up to 3% difference while highest resolution agrees within 0.3%. Fig. 7(b) shows ω/G for $\gamma = 0.5$, 0.25 and 0.125 at a spatial resolution of 14385 particles. While the results with $\gamma = 0.5$ and $\gamma = 0.125$ remain within 1% of those with $\gamma = 0.25$, the simulations with $\gamma = 0.5$ fail to converge for $Re > 8$. As a result, $J_d = 14385$ and $\gamma = 0.25$ are chosen for this case.

When suspended in unbound linear shear, the disc is known to attain a dimensionless angular velocity of $\omega/G = 0.5$. At higher values of Re_p , ω/G decreases linearly with Re_p with a slope of -0.5 [47,63]. This trend holds qualitatively for finite confinement ratios as well, where the general behavior of the angular velocity consists of an initial plateau followed by a gradual decline at higher Re_p (Fig. 8(a)). Our simulations show excellent agreement with prior numerical results by Ding and Aidun [47], Yan et al. [46] and Pan et al. [24] and experimental data by Zettner and Yoda [7]. Fig. 8(b) provides

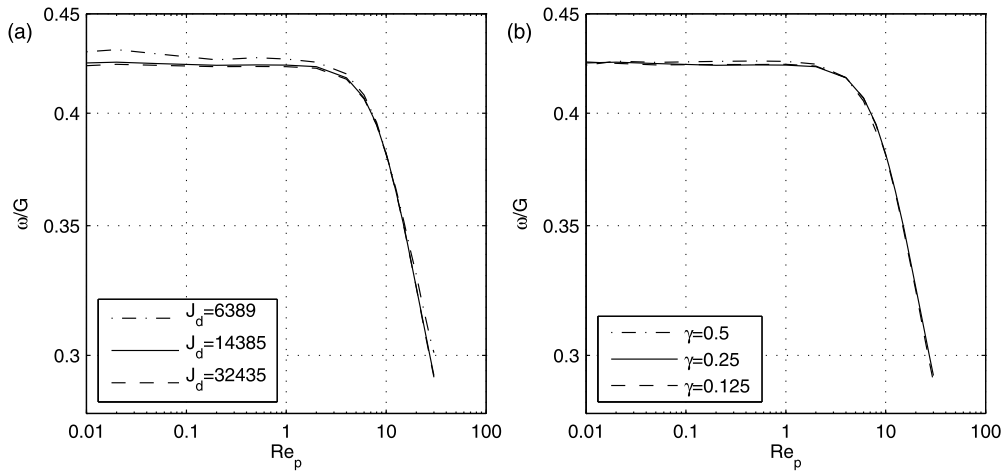


Fig. 7. Comparison of ω/G of case SDR for different spatial resolutions at $\gamma = 0.25$ (a) and different CFL condition constant at $J_d = 62230$ (b).

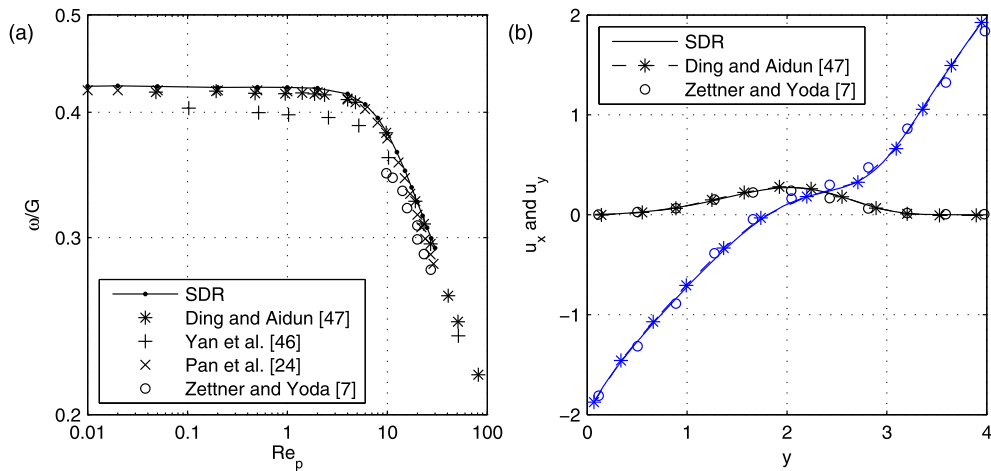


Fig. 8. (a) Comparison of normalized angular velocity versus Re_p ; (b) comparison of streamwise (blue) and normal (black) velocity profiles at 1.85 to the right of the rigid disc's center at $Re_p = 20$; refer to Ding and Aidun [47] for experimental data by Zettner and Yoda [7].

streamwise and normal components of the velocities at $Re_p = 20$. Streamwise velocity is skewed toward $y > 2$ where the flow accelerates as it leaves the vicinity of the disc. The normal component is skewed toward $y < 2$ and represents a flow in the reverse direction of the linear velocity of the disc. Both profiles are in good agreement with numerical and experimental data provided by [47].

Fig. 9 shows the streamlines inside and outside of the rigid disc for Re_p of 0.02 and 20. Particle positions are shown in the background while perceived boundary of the rigid body is shown by 0.5 level contour of the smoothed color function. The streamlines shown may be divided into three types. Those that travel across the periodic boundaries contribute a positive torque to rotate the disc by passing between the moving wall and rigid body. Reversing streamlines change direction in the vicinity of the disc and oppose its rotation while closed streamlines move around the disc. As Re_p increases the streamlines become skewed in the direction of rotation and reversing and closing streamlines draw closer to one another. Similar patterns have been observed in numerical and experimental results as well [7,46,47].

3.4. Single disc migration

To assess the interaction of combined linear and angular motion in the absence of any body force, migration of a neutrally buoyant rigid disc in plane Couette flow is simulated. When released from a distance c from the middle of the channel, it is expected that the disc will migrate toward the centerline while moving with the flow. A schematic of this case is provided in Fig. 1(d). Dimensionless numbers governing this test case are similar to those of case SDR with an additional distance to radius ratio of c/r . Computational domain consists of an 8×32 rectangle discretized by 14402 particles initially arranged similar to the case SDD such that 9 concentric circles cover inside the rigid disc. The confinement ratio is $H/r = 8$. Boundary and initial conditions are similar to case SDR.

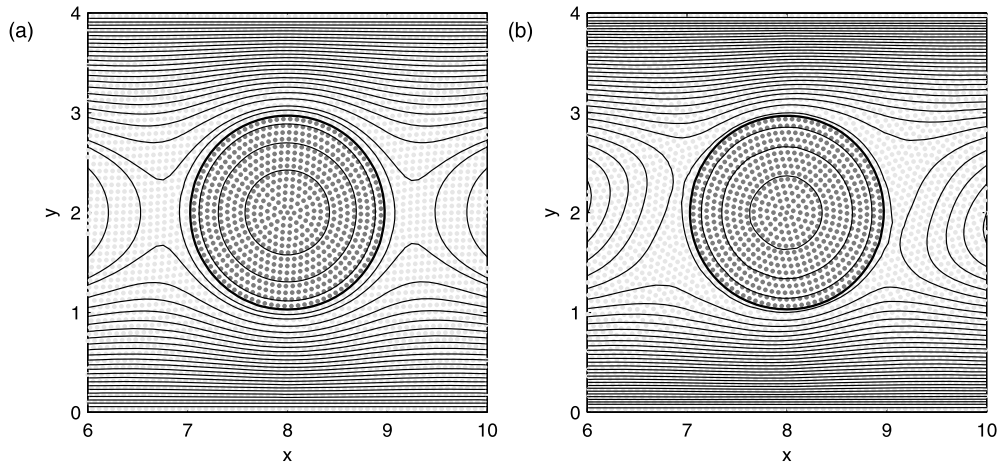


Fig. 9. Streamlines in the vicinity of the disc; particle positions inside the rigid body (dark) and fluid phase (light) are shown in the background. Rigid body boundary is defined as 0.5 level contour of the smoothed color function and is marked by the thicker line. (a) $Re_p = 0.02$; (b) $Re_p = 20$.

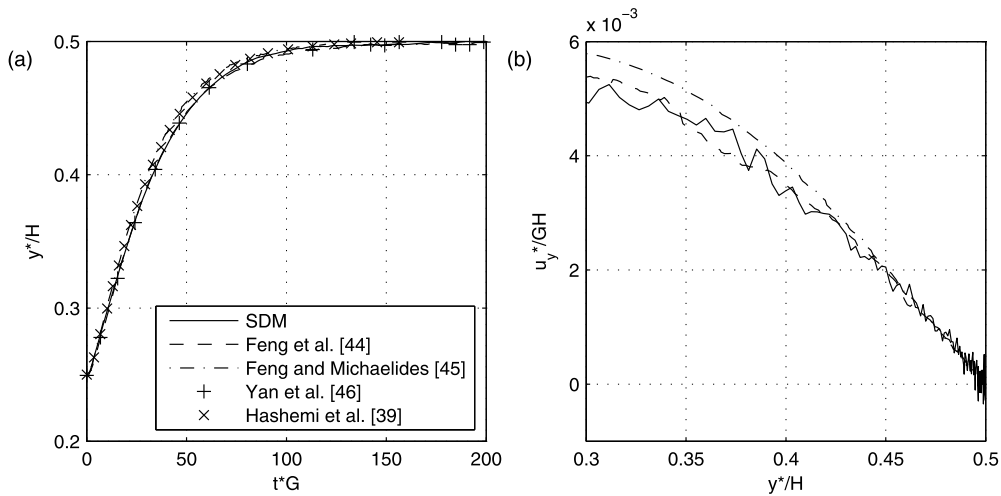


Fig. 10. Comparison of vertical position with respect to time (a) and normal velocity with respect to vertical position (b).

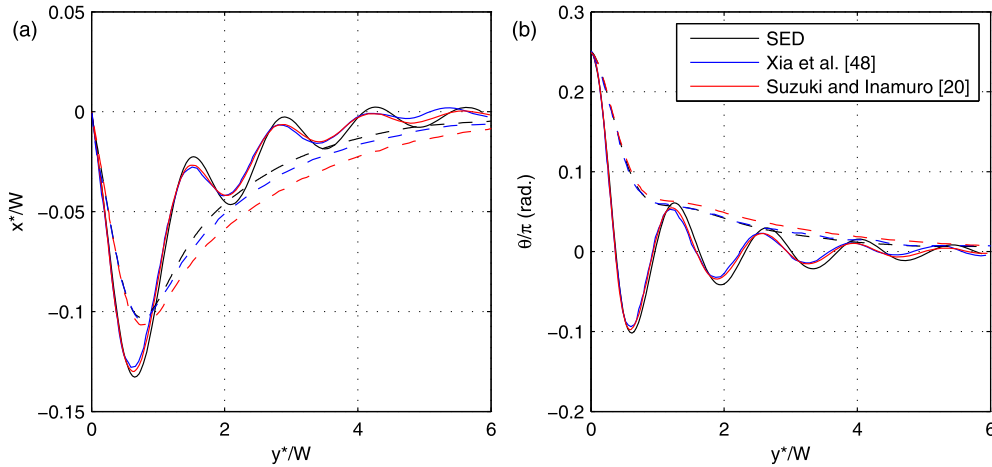
To compare with Feng et al. [44], Feng and Michaelides [45], Yan et al. [46] and Hashemi et al. [39], Re_p and Re_b are set equal to 0.625 and 40, respectively. The symmetry of the migration trajectories from either half of the channel are tested and the position and velocity of the discs were found to agree to within 10^{-3} . The effect of initial slip velocity has also been examined and no significant changes were observed. As a result, the disc is released from $c/r = 2$ below channel centerline with zero initial velocity. Fig. 10 provides normal position and normal velocity of the disc during its migration toward the center of the channel. The positions are in excellent agreement with literature data. The normal velocity exhibits small-amplitude oscillation superimposed on a gradual decline, similar in magnitude to previous calculations in [44]. In contrast, [45] presents a smooth curve with slightly larger magnitude.

3.5. Single ellipse descent

A rigid ellipse sedimenting in a quiescent fluid may present drastically different patterns of motion depending on the channel width, initial angle and positioning of the elliptic disc [43,48]. In this study, two cases at moderate and low Re are simulated and compared to the results provided by Xia et al. [48] and Suzuki and Inamuro [20]. A schematic view of the test case is provided in Fig. 1(e). Dimensionless parameters governing this test case are Re , \mathcal{D} , aspect ratio a/b , blockage ratio W/a and h/l_c . Characteristic length and velocity scales are defined as $l_c = d = \sqrt{ab}$ and $u_c = \sqrt{gd}$, resulting in a Reynolds number defined as $Re_p = \rho_f \sqrt{gd^3} / \mu_f$. For comparison with literature data, we also define an alternative Reynolds number $Re_t = \rho_f u_t a / \mu_f$ based on the major axis of the ellipse a and its terminal descent velocity u_t . Simulation parameters are listed in Table 4. Density ratios covered in this study are low enough to achieve a steady terminal descent velocity until $y^*/W = 3$ [48]. The computational domain consists of a 45.25×5.65 rectangle discretized by 80035 particles while the

Table 4Simulation parameters and Re_t for SED and numerical simulations of Xia et al. [48] and Suzuki and Inamuro [20].

Case	\mathcal{D}	SED		[48]	[20]
		Re_p	Re_t	Re_t	Re_t
1	1.01	58.8	2.15	2.08	1.92
2	1.1	58.8	13.5	12.9	12.6

**Fig. 11.** Comparison of horizontal position (a) and orientation of the ellipse (b) versus vertical position for $\mathcal{D} = 1.01$ (--) and $\mathcal{D} = 1.1$ (—).

center of the ellipse is placed at $h/d = 40$ with an angle of $\theta = \pi/4$. The aspect ratio and blockage ratio are set to 2 and 4, respectively. Boundary conditions are similar to that of case SDD.

The rigid body is discretized such that a relatively uniform particle distribution is achieved in the transition region where the solid particles are within the support domain of the fluid particles. To this end, the rigid body is divided into concentric ellipses, each obtained by shrinking the vertices of the outer ellipse inward by the particle spacing δ_p . The innermost ellipse thus has a minor axis thinner than $2\delta_p$. Particles are placed along the perimeters of all the concentric ellipses at uniform spacing δ_p . If the minor axis of the innermost ellipse is smaller than δ_p , particles are placed along the major axis of this ellipse instead of its perimeter. The resolution given above results in 7 concentric ellipses. Fluid particles are arranged in an equally spaced Cartesian grid.

Fig. 11 plots the horizontal position and the orientation of the ellipse versus the vertical position of its center of mass. At $\mathcal{D} = 1.01$, the three simulations agree quite well in general. But SED and [48] agree very closely, while [20] deviates more from the other two. All cases end up at the middle of the channel in a horizontal position. At $\mathcal{D} = 1.1$, the ellipse tends to have an oscillatory motion that damps out at later stages, leaving the ellipse in a horizontal position at the center of the channel descending at constant velocity. While SED shows a slightly larger amplitude than the other two solutions, the difference is comparable to that between [48] and [20] for $\mathcal{D} = 1.01$. Due to oscillatory nature of the flow, the error of the current solution is compounded at each extrema until the motion damps out. Despite this, the characteristic behavior and final configuration of the ellipse are captured accurately. Table 4 provides Re_t for SED and reference simulations. In both \mathcal{D} , SED predicts the largest Re_t while [20] has the smallest.

4. Conclusions

A two-dimensional smoothed particle hydrodynamics method has been presented for simulation of motion of rigid bodies in Newtonian fluids. The method treats all phases as liquids of different viscosity while applying rigidity constraints to particles within the solid body. As a result, the interpolation scheme and viscosity ratio may affect the accuracy and robustness of the scheme. Descent of a rigid disc in quiescent medium is simulated and weighed harmonic interpolation in conjunction with a viscosity ratio of 100 is found to provide consistently satisfactory results.

In order to fully measure the performance of the proposed method, several test cases involving linear motion, rotational motion and their combination are simulated. The sedimentation of a single disc and a pair of discs are used to measure the performance of the method in simulating linear motion and near contact situations where interpolation regions overlap. A repulsive force based on the color information available to the particles is developed and successfully tested. Rotation of a neutrally buoyant disc in Couette flow is tested to measure the performance of the method in rotational motion. The results within the test range are in quantitative agreement with the literature data. Combined linear and rotational motion is tested by simulating the migration of a neutrally buoyant circular disc placed off center in Couette flow and sedimentation of an

elliptic particle in quiescent medium under gravity. Results of both cases are found to be compatible with the findings of the literature.

The presented scheme aims to extend the simulation capabilities of ISPH for particulate flows. It provides a simple means of handling moving boundaries and is easily extended to multiple bodies using the repulsive force formulated. The agreement between simulation results and literature data shows the ability of our scheme in handling the complex motion of rigid particles in a variety of flow configurations.

Acknowledgements

The authors gratefully acknowledge financial support provided by the Scientific and Technological Research Council of Turkey (TUBITAK) for grant number 112M721 and by the Natural Sciences and Engineering Research Council of Canada (NSERC) for grant number 05862.

References

- [1] E.H. Dowell, K.C. Hall, Modeling of fluid–structure interaction, *Annu. Rev. Fluid Mech.* 33 (2001) 445–490.
- [2] Z.S. Yu, A DLM/FD method for fluid/flexible-body interactions, *J. Comput. Phys.* 207 (2005) 1–27.
- [3] A.A. Shirgaonkar, M.A. MacIver, N.A. Patankar, A new mathematical formulation and fast algorithm for fully resolved simulation of self-propulsion, *J. Comput. Phys.* 228 (2009) 2366–2390.
- [4] G. Oger, M. Doring, B. Alessandrini, P. Ferrant, Two-dimensional SPH simulations of wedge water entries, *J. Comput. Phys.* 213 (2006) 803–822.
- [5] A. Skillen, S. Lind, P.K. Stansby, B.D. Rogers, Incompressible smoothed particle hydrodynamics (SPH) with reduced temporal noise and generalised Fickian smoothing applied to body–water slam and efficient wave–body interaction, *Comput. Methods Appl. Mech. Eng.* 265 (2013) 163–173.
- [6] X. Liu, P. Lin, S. Shao, An ISPH simulation of coupled structure interaction with free surface flows, *J. Fluids Struct.* 48 (2014) 46–61.
- [7] C.M. Zettner, M. Yoda, The circular cylinder in simple shear at moderate Reynolds numbers: an experimental study, *Exp. Fluids* 30 (2001) 346–353.
- [8] K. Sugiyama, S. Ii, S. Takeuchi, S. Takagi, Y. Matsumoto, A full Eulerian finite difference approach for solving fluid–structure coupling problems, *J. Comput. Phys.* 230 (2011) 596–627.
- [9] S. Vincent, J.C.B. de Motta, A. Sarthou, J.-L. Estivalezes, O. Simonin, E. Climent, A Lagrangian VOF tensorial penalty method for the DNS of resolved particle-laden flows, *J. Comput. Phys.* 256 (2014) 582–614.
- [10] C.D. Eggleton, A.S. Popel, Large deformation of red blood cell ghosts in a simple shear flow, *Phys. Fluids* 10 (1998) 1834–1845.
- [11] C. Pozrikidis, Axisymmetric motion of a file of red blood cells through capillaries, *Phys. Fluids* 17 (2005).
- [12] C.S. Peskin, Flow patterns around heart valves: a numerical method, *J. Comput. Phys.* 10 (1972) 252–271.
- [13] H. Watanabe, S. Sugiura, H. Kafuku, T. Hisada, Multiphysics simulation of left ventricular filling dynamics using fluid–structure interaction finite element method, *Biophys. J.* 87 (2004) 2074–2085.
- [14] T.N. Randrianarivelo, G. Pianet, S. Vincent, J.P. Caltagirone, Numerical modelling of solid particle motion using a new penalty method, *Int. J. Numer. Methods Fluids* 47 (2005) 1245–1251.
- [15] C.W. Hirt, A.A. Amsden, J.L. Cook, An arbitrary Lagrangian–Eulerian computing method for all flow speeds, *J. Comput. Phys.* 14 (1974) 227–253.
- [16] T.J.R. Hughes, W.K. Liu, T.K. Zimmermann, Lagrangian–Eulerian finite-element formulation for incompressible viscous flows, *Comput. Methods Appl. Mech. Eng.* 29 (1981) 329–349.
- [17] C.S. Peskin, The immersed boundary method, *Acta Numer.* 11 (2002) 479–517.
- [18] M. Uhlmann, An immersed boundary method with direct forcing for the simulation of particulate flows, *J. Comput. Phys.* 209 (2005) 448–476.
- [19] J. Yang, F. Stern, Sharp interface immersed-boundary/level-set method for wave–body interactions, *J. Comput. Phys.* 228 (2009) 6590–6616.
- [20] K. Suzuki, T. Inamuro, Effect of internal mass in the simulation of a moving body by the immersed boundary method, *Comput. Fluids* 49 (2011) 173–187.
- [21] R. Mittal, G. Iaccarino, Immersed boundary methods, *Annu. Rev. Fluid Mech.* 37 (2005) 239–261.
- [22] R. Glowinski, T.W. Pan, T.I. Hesla, D.D. Joseph, J. Periaux, A fictitious domain approach to the direct numerical simulation of incompressible viscous flow past moving rigid bodies: application to particulate flow, *J. Comput. Phys.* 169 (2001) 363–426.
- [23] N.A. Patankar, P. Singh, D.D. Joseph, R. Glowinski, T.W. Pan, A new formulation of the distributed Lagrange multiplier/fictitious domain method for particulate flows, *Int. J. Multiph. Flow* 26 (2000) 1509–1524.
- [24] T.-W. Pan, S.-L. Huang, S.-D. Chen, C.-C. Chu, C.-C. Chang, A numerical study of the motion of a neutrally buoyant cylinder in two dimensional shear flow, *Comput. Fluids* 87 (2013) 57–66.
- [25] P. Angot, C.H. Bruneau, P. Fabrie, A penalization method to take into account obstacles in incompressible viscous flows, *Numer. Math.* 81 (1999) 497–520.
- [26] K. Khadra, P. Angot, S. Parneix, J.P. Caltagirone, Fictitious domain approach for numerical modelling of Navier–Stokes equations, *Int. J. Numer. Methods Fluids* 34 (2000) 651–684.
- [27] J.B. Ritz, J.P. Caltagirone, A numerical continuous model for the hydrodynamics of fluid particle systems, *Int. J. Numer. Methods Fluids* 30 (1999) 1067–1090.
- [28] S. Vincent, T.N. Randrianarivelo, G. Pianet, J.-P. Caltagirone, Local penalty methods for flows interacting with moving solids at high Reynolds numbers, *Comput. Fluids* 36 (2007) 902–913.
- [29] M.B. Liu, G.R. Liu, Smoothed Particle Hydrodynamics (SPH): an overview and recent developments, *Arch. Comput. Methods Eng.* 17 (2010) 25–76.
- [30] P. Koumoutsakos, Multiscale flow simulations using particles, *Annu. Rev. Fluid Mech.* 37 (2005) 457–487.
- [31] L.B. Lucy, A numerical approach to the testing of the fission hypothesis, *Astron. J.* 82 (1977) 1013–1024.
- [32] R.A. Gingold, J.J. Monaghan, Smoothed particle hydrodynamics: theory and application to non-spherical stars, *Mon. Not. R. Astron. Soc.* 181 (1977) 375–389.
- [33] S. Shao, Incompressible SPH simulation of water entry of a free-falling object, *Int. J. Numer. Methods Fluids* 59 (2009) 91–115.
- [34] B. Bouscasse, A. Colagrossi, S. Marrone, M. Antuono, Nonlinear water wave interaction with floating bodies in SPH, *J. Fluids Struct.* 42 (2013) 112–129.
- [35] A. Colagrossi, G. Colicchio, C. Lugni, M. Brocchini, A study of violent sloshing wave impacts using an improved SPH method, *J. Hydraul. Res.* 48 (2010) 94–104.
- [36] M. Ozbulut, M. Yildiz, O. Goren, A numerical investigation into the correction algorithms for SPH method in modeling violent free surface flows, *Int. J. Mech. Sci.* 79 (2014) 56–65.
- [37] S.E. Hieber, P. Koumoutsakos, An immersed boundary method for smoothed particle hydrodynamics of self-propelled swimmers, *J. Comput. Phys.* 227 (2008) 8636–8654.

- [38] S. Marrone, A. Colagrossi, M. Antuono, G. Colicchio, G. Graziani, An accurate SPH modeling of viscous flows around bodies at low and moderate Reynolds numbers, *J. Comput. Phys.* 245 (2013) 456–475.
- [39] M.R. Hashemi, R. Fatehi, M.T. Manzari, A modified SPH method for simulating motion of rigid bodies in Newtonian fluid flows, *Int. J. Non-Linear Mech.* 47 (2012) 626–638.
- [40] X. Bian, M. Ellero, A splitting integration scheme for the SPH simulation of concentrated particle suspensions, *Comput. Phys. Commun.* 185 (2014) 53–62.
- [41] M.S. Shadloo, A. Zainali, M. Yildiz, A. Suleman, A robust weakly compressible SPH method and its comparison with an incompressible SPH, *Int. J. Numer. Methods Eng.* 89 (2012) 939–956.
- [42] E.S. Lee, C. Moulinec, R. Xu, D. Violeau, D. Laurence, P. Stansby, Comparisons of weakly compressible and truly incompressible algorithms for the SPH mesh free particle method, *J. Comput. Phys.* 227 (2008) 8417–8436.
- [43] J. Feng, H.H. Hu, D.D. Joseph, Direct simulation of initial-value problems for the motion of solid bodies in a Newtonian fluid. 1. Sedimentation, *J. Fluid Mech.* 261 (1994) 95–134.
- [44] J. Feng, H.H. Hu, D.D. Joseph, Direct simulation of initial-value problems for the motion of solid bodies in a Newtonian fluid. 2. Couette and Poiseuille flows, *J. Fluid Mech.* 277 (1994) 271–301.
- [45] Z.G. Feng, E.E. Michaelides, The immersed boundary-lattice Boltzmann method for solving fluid–particles interaction problems, *J. Comput. Phys.* 195 (2004) 602–628.
- [46] Y. Yan, J.F. Morris, J. Koplik, Hydrodynamic interaction of two particles in confined linear shear flow at finite Reynolds number, *Phys. Fluids* 19 (2007).
- [47] E.J. Ding, C.K. Aidun, The dynamics and scaling law for particles suspended in shear flow with inertia, *J. Fluid Mech.* 423 (2000) 317–344.
- [48] Z. Xia, K.W. Connington, S. Rapaka, P. Yue, J.J. Feng, S. Chen, Flow patterns in the sedimentation of an elliptical particle, *J. Fluid Mech.* 625 (2009) 249–272.
- [49] S.J. Cummins, M. Rudman, An SPH projection method, *J. Comput. Phys.* 152 (1999) 584–607.
- [50] S. Koshizuka, A. Nobe, Y. Oka, Numerical analysis of breaking waves using the moving particle semi-implicit method, *Int. J. Numer. Methods Fluids* 26 (1998) 751–769.
- [51] J.P. Morris, A study of the stability properties of smooth particle hydrodynamics, *Publ. Astron. Soc. Aust.* 13 (1996) 97–102.
- [52] M.S. Shadloo, A. Zainali, S.H. Sadek, M. Yildiz, Improved incompressible smoothed particle hydrodynamics method for simulating flow around bluff bodies, *Comput. Methods Appl. Mech. Eng.* 200 (2011) 1008–1020.
- [53] J.J. Monaghan, J.C. Lattanzio, A refined particle method for astrophysical problems, *Astron. Astrophys.* 149 (1985) 135–143.
- [54] J.J. Monaghan, A. Kocharyan, SPH simulation of multiphase flow, *Comput. Phys. Commun.* 87 (1995) 225–235.
- [55] S.D. Shao, E.Y.M. Lo, Incompressible SPH method for simulating Newtonian and non-Newtonian flows with a free surface, *Adv. Water Resour.* 26 (2003) 787–800.
- [56] A. Zainali, N. Tofighi, M.S. Shadloo, M. Yildiz, Numerical investigation of Newtonian and non-Newtonian multiphase flows using ISPH method, *Comput. Methods Appl. Mech. Eng.* 254 (2013) 99–113.
- [57] R. Xu, P. Stansby, D. Laurence, Accuracy and stability in incompressible SPH (ISPH) based on the projection method and a new approach, *J. Comput. Phys.* 228 (2009) 6703–6725.
- [58] M. Yildiz, R.A. Rook, A. Suleman, SPH with the multiple boundary tangent method, *Int. J. Numer. Methods Eng.* 77 (2009) 1416–1438.
- [59] N. Tofighi, M. Ozbulut, A. Rahmat, M. Yildiz, J.J. Feng, Descent of a solid disk in quiescent fluid simulated using incompressible smoothed particle hydrodynamics, in: E. Onate, J. Oliver, A. Huerta (Eds.), *Proc. WCCM XI*, vol. 5, 2014, pp. 5310–5318.
- [60] A.J.C. Ladd, Numerical simulations of particulate suspensions via a discretized Boltzmann-equation. 2. Numerical results, *J. Fluid Mech.* 271 (1994) 311–339.
- [61] M. Coquerelle, G.H. Cottet, A vortex level set method for the two-way coupling of an incompressible fluid with colliding rigid bodies, *J. Comput. Phys.* 227 (2008) 9121–9137.
- [62] Z. Zhang, A. Prosperetti, A method for particle simulation, *J. Appl. Mech.* 70 (2003) 64–74.
- [63] C.A. Kossack, A. Acrivos, Steady simple shear flow past a circular cylinder at moderate Reynolds numbers: a numerical solution, *J. Fluid Mech.* 66 (1974) 353–376.